ACS OMEGA

Open Access

http://pubs.acs.org/journal/acsodf

Article

Reaction Atmosphere-Controlled Thermal Conversion of Ferrocene to Hematite and Cementite Nanomaterials—Structural and Spectroscopic Investigations

Sani Kundu, Toton Sarkar, Gurupada Ghorai, Pratap K. Sahoo, Ahmad Aziz Al-Ahmadi, Ahmad Alghamdi, and Ashis Bhattacharjee*

Cite This: *ACS Omega* 2024, 9, 22607−22618

Read Online

ACCESS | Metrics & More | Article Recommendations

ABSTRACT: Recently, we have reported the influence of various reaction atmospheres on the solid-state reaction kinetics of ferrocene, where oxalic acid dihydrate was used as a coprecursor. In this light, present study discusses on the nature of decomposed materials of the solid-state reactions of ferrocene in O_2, air, and N_2 atmospheres. The ambient and oxidative atmospheres caused the decomposition to yield pure hematite nanomaterials, whereas cementite nanomaterials along with α-Fe were obtained in N_2 atmosphere. The obtained materials were mostly agglomerated. Elemental composition of each material was estimated. Using the absorbance data, the energy band gap values were estimated and the related electronic transitions from the observed absorption spectra were explored. Urbach energy was calculated for hematite, which described the role of defects in the decomposed materials. The nanostructures exhibited photoluminescence due to self-trapped states linked to their optical characteristics. Raman spectroscopy of hematite detected seven Raman modes, confirming the rhombohedral structure, whereas the D and G bands were visible in the Raman spectra for cementite. Thus, the reaction atmosphere significantly influenced the thermal decomposition of ferrocene and controls the type of nanomaterials obtained. Plausible reactions of the undergoing solid-state decomposition have been proposed.

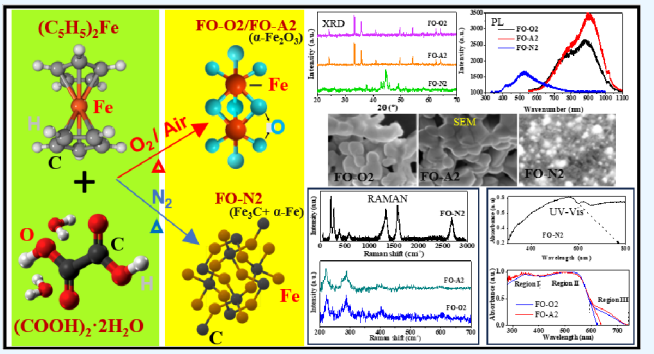

1. INTRODUCTION

Over the last few decades, iron-based nanomaterials have been drawing huge research due to their wide range applications, including catalysis, data storage, environmental remediation, disease diagnostics, and therapy.[1−5] Among different known iron oxides, hematite (α-Fe_2O_3) nanostructures are popular due to their unique properties and uses in many different sectors.[1,4,6−10] Hematite, with its corundum rhombohedral structure, is found to be the most stable iron oxide in an ambient atmosphere. Additionally, it can serve as the starting material for the production of magnetite (Fe_3O_4) and maghemite (γ-Fe_2O_3).[11] Hematite with bandgap of around 2.2 eV, acts as an n-type semiconductor and possesses a magnetic spin-flop transition at ∼260 K.[12] Conversely, iron carbides have found useful applications in different fields, particularly because of their magnetic, catalytic, and mechanical properties.[2,5,13,14] Structurally, they are intermetallic compounds consisting of iron and carbon that range in composition from FeC to Fe_7C. Among these different forms of iron carbides, cementite (Fe_3C) is the most popular, and it possesses an orthorhombic crystal structure and huge application potential.[3,15−17] Study of iron carbide materials in the nanometric range is a complex as well as challenging part of research because of the delicate balance among the various phases of the dominant components.

Organoiron compound ferrocene, $(C_5H_5)_2Fe$, has been used profusely either as a precursor or catalyst for synthesis of various iron-based nanostructures.[18−,27,28−31] Ferrocene, solid at room temperature with mp at ∼450 K and bp at ∼522 K, undergoes complete sublimation.[32] Above ∼773 K, ferrocene vapor decomposes to metallic iron along with several gaseous products (e.g., CH_4, H_2).[33] However, under inert and oxidative atmospheres, the sublimation occurs below 500 K.[34] Remarkably, the presence of oxalic acid dihydrate $(COOH)_2 \cdot 2H_2O$ stops the sublimation of ferrocene and yields hematite below 450 K in air.[29] Notably, bare oxalic acid dihydrate

Received: December 24, 2023
Revised: March 20, 2024
Accepted: April 10, 2024
Published: May 16, 2024

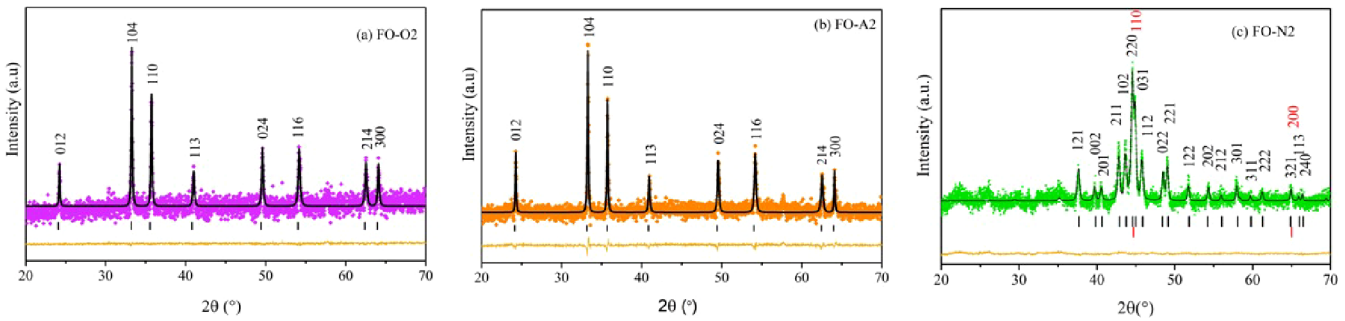

Figure 1. Powder XRD patterns of the decomposed samples along with the Rietveld refinements: (a) FO-O2, (b) FO-A2, and (c) FO-N2 samples.

decomposes completely when heated over 373 K.[35] Conversely, ferrocene also plays a vital role in preparing Fe_3C nanostructures.[20−27]

As properties of nanoparticles are highly influenced by their size, shape, surface area, and in-built crystalline defects which provide opportunities for their uses,[36] there are a variety of techniques used for the synthesis of iron-based nanoparticles, including sol−gel, coprecipitation, hydrothermal, green synthesis, and thermal decomposition. We concentrate on the thermal decomposition technique because it provides simple control over the product's purity, phase, composition, microstructure, and other aspects of the process.[11] This technique has a number of benefits, such as quick reaction time, relatively low temperature of formation, and possibility of using innocuous compounds. The characteristics of the products are affected by the reaction time, temperature, environment, and chemical nature of the precursors utilized. It was worthwhile to investigate the effect of different reaction atmospheres on the solid-state reaction of ferrocene in the presence of oxalic acid dihydrate, and in this light, recently, we reported a reaction kinetic study.[37,38] Extending our research further, focus of the present paper is to explore on the nature of materials obtained on the solid-state reaction of ferrocene in the presence of oxalic acid dihydrate in O_2, air, and N_2 atmospheres. The synthesized materials were characterized by powder XRD, FE-SEM, EDX, HR-TEM, UV−vis−NIR, photoluminescence, and Raman spectroscopy. It was established that the synthesized materials are in the nanometric range and are hematite in O_2 and air atmospheres, but majorly cementite under N_2 atmosphere. It is evident from the observations that the reaction atmosphere has a significant impact on the solid-state reaction of ferrocene in the presence of oxalic acid dihydrate. The present study exemplifies the role of reaction atmosphere on thermal decomposition leading to various iron-based nanomaterials using the same precursor.

2. RESULTS AND DISCUSSION

2.1. Structure and Morphology Studies. Powder XRD patterns of the as-grown samples obtained on thermal decomposition of 1:1 mixture of ferrocene and oxalic acid dihydrate in O_2, air, and N_2 atmospheres did not show pure crystalline phases, which when annealed in respective gaseous environments at 500 °C for 2 h also did not exhibit pure crystalline phases. This led to further annealing of these samples for another 2 h at 750 °C, and the resulting materials in O_2, air, and N_2 atmospheres, i.e. FO-O2, FO-A2, and FO-N2, exhibited perfect crystalline phases. Figure 1 presents the room temperature XRD patterns of FO-O2, FO-A2, and FO-N2 obtained in the $20° < 2\theta < 70°$ range along with the Rietveld refinement, where the dot and the line represent the observed data and the calculated pattern while the vertical bars indicate the Bragg diffraction positions. The curve at the bottom panel shows the difference between the observed and calculated patterns. These samples exhibit strong narrow sharp peaks in the XRD patterns, confirming the high degree of crystallinity. FullProf program was used to study the structure. According to XRD analysis, FO-O2 and FO-A2 are found to be pure hematite (α-Fe_2O_3) (COD-96−901−5066) with rhombohedral symmetry (space group: $R3c$), while FO-N2 matches to a mixture of Fe_3C−cementite phase (COD-96−901−2189) with orthorhombic structure (space group $Pnma$) and α-Fe (COD-96−500−0218) with cubic structure (space group: $Im\bar{3}m$). In the XRD profile of FO-O2 and FO-A2, two characteristic strong peaks at (104) and (110) and other peaks at (012), (113), (024), (116), (214), and (300) corresponding to hematite are observed. Conversely, the XRD profile of FO-N2 shows five strong peaks corresponding to cementite (211), (102), (220), (031), (112) and some other typical weak peaks of cementite at (121), (002), (201), (301), (022), (221) along with peaks corresponding to α-Fe (strong (110) peak with $2\theta = 44.679°$ and the (200) peak with $2\theta = 65.031°$). Notably, neither any trace of cementite or α-Fe was traced in FO-O2 and FO-A2 nor the presence of any iron oxide was evidenced in FO-N2. Thus, from XRD analysis it is found that thermal decomposition of a 1:1 mixture of ferrocene and oxalic acid dihydrate in oxidative and air atmospheres produces 100% hematite, whereas the same mixture when decomposed under a N_2 atmosphere produces cementite (68%) and α-Fe (32%), which convincingly indicates the impact of the gaseous reaction atmosphere on the thermal conversion of ferrocene. It is known that thermal decomposition of mixture of ferrocene and oxalic acid dihydrate in air[29] produced hematite nanomaterials. On the other hand, the formation of Fe_3C from the pyrolysis of ferrocene or ferrocene/hydrocarbon mixtures was reported.[23−27]

Scherrer formula is popularly employed to estimate the crystallite size from the powder XRD patterns[39]

$$D = \frac{K\lambda}{\beta_{hkl}\cos\theta} \tag{1a}$$

where $K = 0.9$, λ = the wavelength of X-ray used, β_{hkl} = the full width at half-maximum of the diffraction peaks corrected for instrumental broadening (in radian), and θ = the angle of diffraction. However, this formula only takes into account how crystallite size affects the XRD peak profile but does not take any consideration of the intrinsic strain that comes from the grain boundary, point defect, and triple junction in nanocrystals, and as a result, this method generally provides smaller

https://doi.org/10.1021/acsomega.3c10332
ACS Omega 2024, 9, 22607−22618

Table 1. Structural Parameters of FO-O2, FO-A2, and FO-N2 Obtained from Powder X-ray Diffraction Data Analysis

material	identity	Miller indices (hkl)	2θ (deg)	β_{hkl} (deg)	d_{hkl} (Å)	D (nm) (eq 1a)	lattice parameters (Å)	V (Å^3)
FO-O2	hematite (100%)	012	24.166	0.179	3.680	45.387	a = 5.0323	301.2530
		104	33.187	0.192	2.697	43.175	c = 13.7364	
		110	35.654	0.197	2.516	42.360		
		113	40.892	0.207	2.205	40.959		
		024	49.501	0.227	1.840	38.537		
		116	54.117	0.239	1.693	37.325		
		214	62.484	0.263	1.485	35.330		
		300	64.046	0.268	1.453	34.963		
FO-A2	hematite (100%)	012	24.15	0.129	3.682	62.977	a = 5.0369	302.1819
		104	33.16	0.134	2.699	61.858	c = 13.7536	
		110	35.63	0.136	2.517	61.356		
		113	40.86	0.140	2.206	60.554		
		024	49.46	0.148	1.841	59.098		
		116	54.06	0.154	1.694	57.912		
		214	62.43	0.165	1.486	56.297		
		300	63.99	0.167	1.453	56.091		
FO-N2	cementite (68.2%)	121	37.659	0.358	2.387	23.425	a = 5.0854b = 6.7404	155.0928
		002	39.814	0.353	2.262	23.960		
		201	40.669	0.350	2.217	24.190	c = 4.5246	
		211	42.915	0.344	2.106	24.848		
		102	43.761	0.341	2.067	25.119		
		220	44.605	0.338	2.030	25.402		
		031	45.013	0.337	2.012	25.543		
		112	45.884	0.334	1.976	25.858		
		022	48.422	0.324	1.878	26.875		
		221	49.156	0.321	1.852	27.201		
		122	51.848	0.309	1.762	28.542		
		202	54.227	0.298	1.690	29.961		
		212	56.051	0.288	1.639	31.240		
		301	58.059	0.276	1.587	32.897		
		311	59.806	0.265	1.545	34.613		
		222	61.309	0.254	1.511	36.357		
		321	64.877	0.224	1.436	42.012		
		113	66.029	0.213	1.414	44.544		
		240	66.514	0.208	1.405	45.762		
	α-Fe (31.8%)	110	44.679	0.332	2.027	25.871	$a = b = c$ = 2.8661	23.5432
		200	65.031	0.200	1.433	47.105		

crystallite size values. XRD peak does not correspond to the Lorentzian function or Gaussian function since the Gaussian function can be well fitted only in the XRD peak region, while the Lorentz function can be fitted well only with the tails. To get rid of this problem and to represent the peak broadening precisely, the Halder–Wagner (H–W) method[40] assumes a symmetric Voigt function—a convolution of Lorentzian and Gaussian functions. So, following the H–W method, for Voigt function, the full width at half-maximum of the XRD profile is written as $\beta_{hkl}^2 = \beta_L\beta_{hkl} + \beta_G^2$, where β_L and β_G are the full width at half-maximum of the Lorentzian and Gaussian functions. The advantage of this method is that it places greater emphasis on the peaks at low and mid angle ranges where there is very little overlap between the diffracting peaks. According to the H–W method, the relation between the crystallite size and lattice strain is given by,

$$\left(\frac{\beta_{hkl}^*}{d_{hkl}^*}\right)^2 = \frac{1}{D}\frac{\beta_{hkl}^*}{d_{hkl}^{*\,2}} + \left(\frac{\epsilon}{2}\right)^2 \quad (1b)$$

where $\beta_{hkl}^* = \beta_{hkl}\cos\theta/\lambda$, $d_{hkl}^* = 2\sin\theta/\lambda$, λ = X-ray wavelength employed, β_{hkl} = the full width at half-maximum of the diffraction peaks, and θ = the angle of diffraction. The H–W method offers significantly higher accuracy.[41] The average strain (ϵ_{strain}) of the materials can be estimated using the Wilson relation[42]

$$\epsilon_{strain} = \frac{\beta_{hkl}}{4\tan\theta} \quad (1c)$$

whereas Williamson and Smallman's formula[43] can be used to calculate the dislocation density (δ) as follows

$$\delta = \frac{1}{D^2} \quad (1d)$$

The estimated values of lattice parameters, Miller indices (hkl) of the diffracting planes, line width β_{hkl}, and interplanar distance (d_{hkl}) are presented in Table 1, whereas in Table 2 the values of crystallite size D and microstrain ϵ_{strain} estimated using eqs 1a, 1b and eqs 1b, 1c, respectively are compared. As expected, the D values estimated following the Scherrer equation are lower than those observed from the H–W equation. The strain values estimated following H–W and Wilson relations are quite comparable and have inverse relation with the crystallite size. For the estimation of

https://doi.org/10.1021/acsomega.3c10332
ACS Omega 2024, 9, 22607−22618

Table 2. Estimated Values of Crystallite Size, Lattice Strain, and Dislocation Density Obtained from Analysis of XRD Data Using Different Methods[a]

	D (nm)		ε (10^{-3})		δ (10^{14}) (line/m^2)
material	eq 1a	eq 1b	eq 1b	eq 1c	eq 1d
FO-O2	39.73	54.43 (54 ± 4)	3.96	2.44	3.37
FO-A2	59.55	71.89 (73 ± 4)	1.68	1.64	1.93
FO-N2	30.44	23.51 (31 ± 5)	-	2.91	18.09
Fe	36.49	24.55	-	2.45	16.59

[a]Values within parentheses are obtained from the FESEM study.

dislocation density δ and following discussions, we considered the results obtained using the H−W method only. A decrease in the β_{hkl} values with increasing crystallite size has been noted, which may be correlated to the strain-induced broadening due to imperfections and the difference in the size of crystallites. Thus, it is clear that starting with same sample thermal decomposition under different gaseous conditions produced various iron-based nanoparticles of varying type and size.

FE-SEM was utilized to estimate the particle size and surface morphologies of the synthesized samples. Figure 2a−c displays the selected FE-SEM images of FO-O2, FO-A2, and FO-N2. FE-SEM images of FO-O2 and FO-A2 reveal that the synthesized materials are clusters of large round-shaped particles with an average diameter of approximately 54 ± 4 nm for FO-O2 and 73 ± 4 nm for FO-A2 obtained from histogram (Figure 2d−f), whereas FO-N2 consists of comparatively smaller particles with 31 ± 5 nm particle size. Completely different views of the particle morphology for FO-N2 are evidenced here. The inserts in Figure 2a−c display the enlarged view of such particles. The irregular surface of particles is often a characteristic of powdery and porous nanomaterials.[44] Large agglomerations in FO-O2 and FO-A2 may be caused by strong van der Waals interactions and magnetic dipole−dipole attraction between the nanoparticles, which is a common occurrence for magnetic nanoparticles.[45] Additionally, elemental study was also performed to verify the purity of the samples by EDX analysis (see inserts in Figure 2d−f). For the EDX spectrum of FO-O2 and FO-A2, the strong peaks observed around 0.7, 6.4, and 7 keV are attributed to the Fe binding energies,[12] whereas the peak at 0.5 keV is assigned to oxygen. The traceable carbon impurity seen is due to carbon tape used in the sample holder. For FO-N2, the presence of Fe and C can be perceived in the EDX spectra, where the strong peak at 0.2 keV is due to C.[46]

The selected TEM images of FO-O2, FO-A2, and FO-N2 are displayed in Figure 3a−c, where large agglomerations of nanoparticles can be observed in the focused zone in the images. Magnetic nanoparticles often exhibit large agglomeration since strong chemical bonds or weak surface forces bind them together. However, the edges of each particle are clearly noticeable regardless of the agglomeration, which indicates that the synthesized hematite nanoparticles FO-O2 and FO-A2 have hexagonal shapes, whereas FO-N2 have irregular shapes. ImageJ software was used to evaluate the particle sizes of the nanoparticles. Thus, obtained particle size distributions are presented in Figure 3 d−f as histograms. The estimated particle size for FO-O2 and FO-A2 ranges from 30 to 100 nm, whereas that for FO-N2 lies between 15 and 55 nm. The particle size distribution can be fitted with Lorentz distribution, where their mean particle sizes are 56 ± 4 nm, 75 ± 4, and 30 ± 5 nm for FO-O2, FO-A2, and FO-N2, respectively, which are close to those observed from XRD and SEM studies. Figure 3g−i displays the HRTEM images of the FO-O2, FO-A2, and FO-N2 nanoparticles. The determined interplanar spacing (d_{hkl}) values for FO-O2 and FO-A2 are found to be 2.516 and 2.699 Å, indicating the (110) and (104) planes, respectively. However, for FO-N2 the interplanar spacing (d_{hkl}) is not clearly visible. Figure 3j−l shows the fast Fourier transform (FFT) diffraction patterns of the FO-O2, FO-A2, and FO-N2 nanoparticles. The bright spot array observed for FO-O2 and

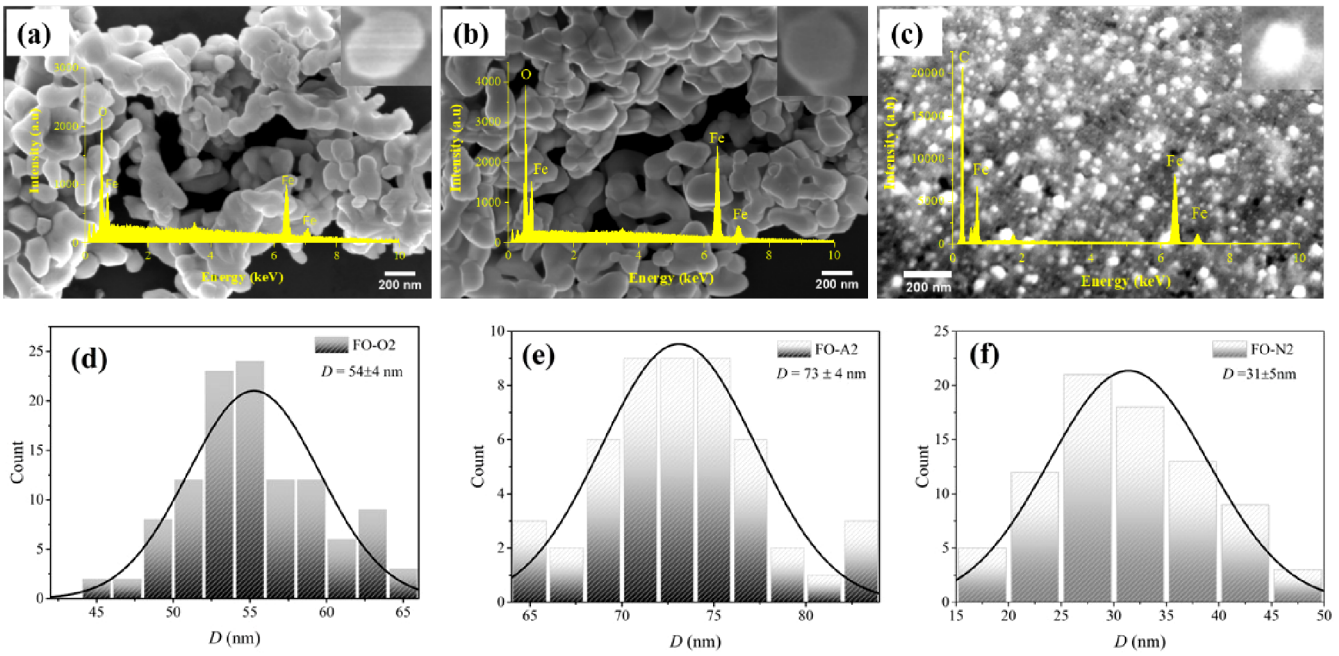

Figure 2. (a-c) SEM images of FO-O2, FO-A2, and FO-N2 with corresponding EDX spectrum as inserts; (d−f) particle size histograms of FO-O2, FO-A2, and FO-N2.

https://doi.org/10.1021/acsomega.3c10332
ACS Omega 2024, 9, 22607−22618

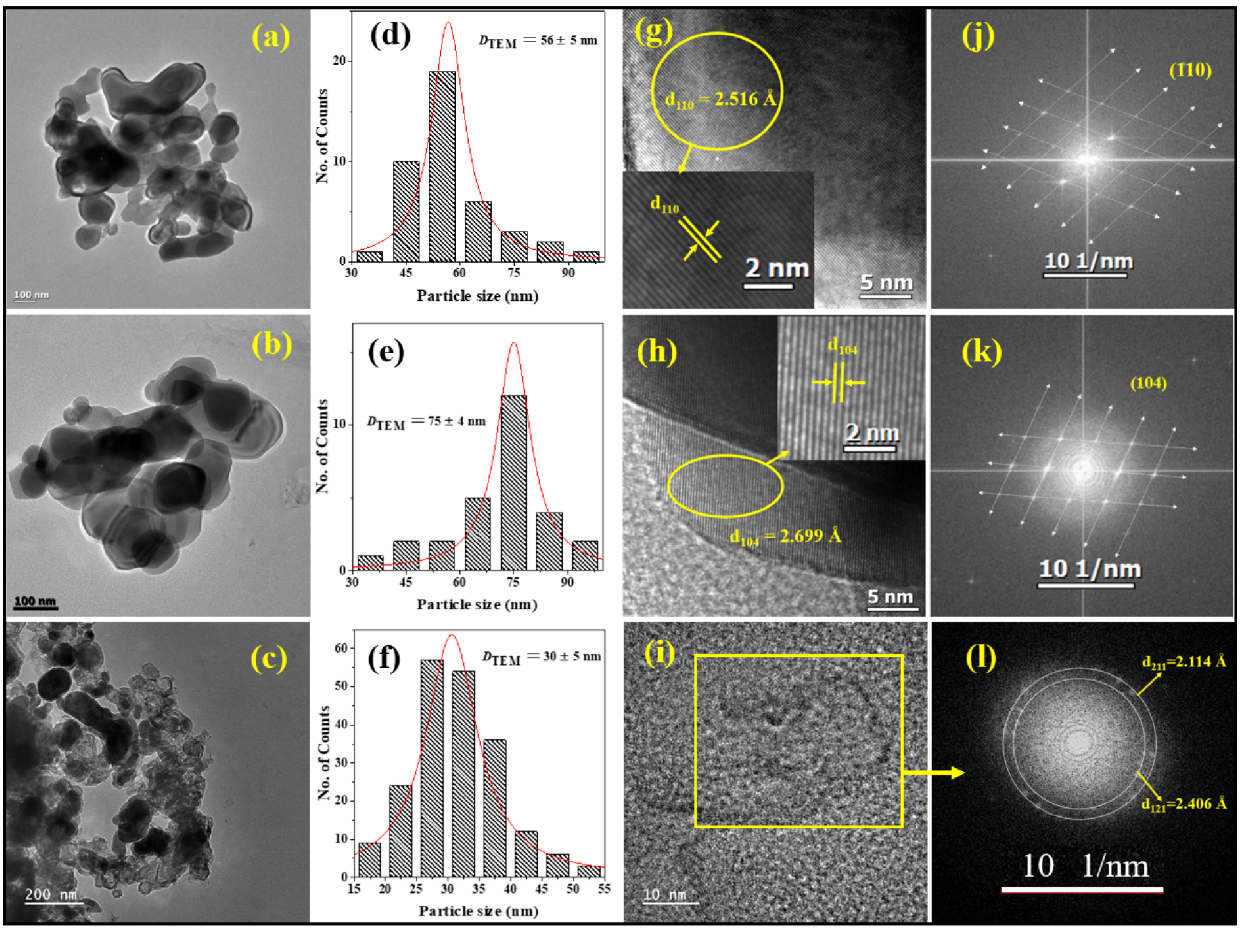

Figure 3. (a–c) TEM images; (d–f) histograms of particle size; (g–i) lattice planes where inserts show the magnified view; (j–l) FFT images of HRTEM images of FO-O2, FO-A2, and FO-N2.

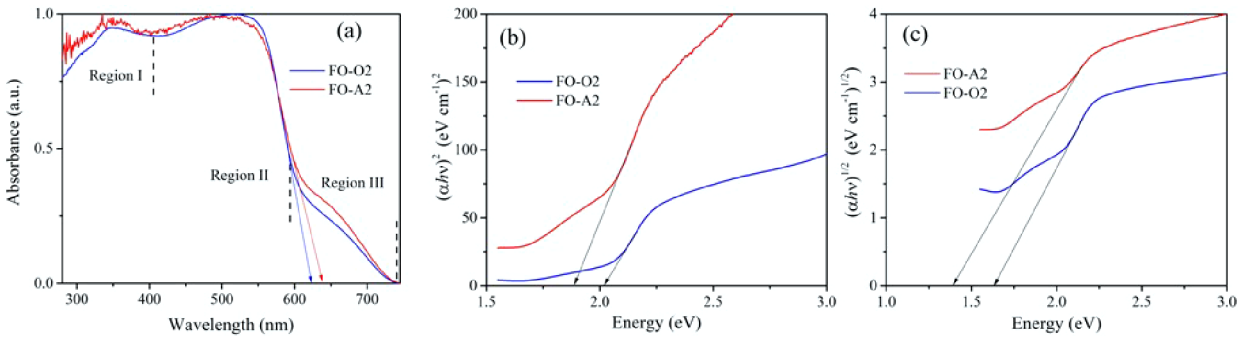

Figure 4. (a) Absorption spectra of FO-O2 and FO-A2 samples; (b) Tauc's plots for n = 2; (c) Tauc's plots for n = 0.5.

FO-A2 indicates the vertical and horizontal alignment of single-crystal-like hematite nanoparticles indexing the (110) and (104) planes. For FO-N2, the circular alignment of bright spot elucidates the polycrystalline nature, where the estimated interplanar spacing (d_{hkl}) values are found to be 2.114 and 2.406 Å, indicating the (211) and (121) planes, respectively. These results are inconsistent with those obtained from the XRD studies.

2.2. Spectroscopic Studies. Figure 4a shows the absorption spectra obtained for FO-O2 and FO-A2 in the wavelength range of 280–800 nm. The optical absorption spectra of iron oxides are well-defined with the aid of crystal field theory.[47] In the hexagonal structure of the hematite crystal, the Fe^{3+} cation forms an octahedral coordination with the O^{2-} anions. The $3d^5$ shell of the octahedrally coordinated Fe^{3+} ions undergo a variety of electronic transitions, like Fe^{3+} ligand field transitions (d–d transition), ligand-to-metal charge-transfer transitions (LMCT), and pair excitations of two magnetically connected adjacent Fe^{3+}centers, that cause the optical absorption.[48] According to the Tanabe Sugano diagram,[49] the 3d atomic orbitals of Fe split into two levels (conventionally denoted as t_{2g} and e_g). Due to exchange energy, these energy levels further split into two sets (one for majority spin and the other for minority spin) giving rise to two sets of t_{2g} and e_g orbitals. The ligand field transitions occur from the ground state to various excited states having different electronic configurations of the orbitals. In the observed absorption spectra, the entire wavelength range can be divided

https://doi.org/10.1021/acsomega.3c10332
ACS Omega 2024, 9, 22607–22618

into three regions corresponding to different electronic transitions (LMCT, ligand field transitions and pair excitations).[49] Region-I (280−400 nm) is assigned to LMCT transitions and ligand field transitions $^6A_1(^6S)$ to $^4T_1(^4P)$ at 290−310 nm, $^6A_1(^6S)$ to $^4E(^4D)$ and $^4T_1(^4D)$ at 360−380 nm.[48,49] Region-II (400−600 nm) corresponds to pair excitation processes from $^6A_1(^6S)$ + $^6A_1(^6S)$ to $^4T_1(^4G)$ + $^4T_1(^4G)$ between two magnetically coupled Fe^{3+}cations at 485−550 nm overlapping the ligand field transition from $^6A_1(^6S)$ to^4E, $^4A_1$ (^4G) at 430 nm.[51] These pair excitation transitions are responsible for the strongest absorption band at 534 nm, which causes the red color of hematite.[49] Region-III (600−750 nm) is corelated to ligand field transition from $^6A_1(^6S)$ to $^4T_2(^4G)$ at 659 nm.[50,52,53] Another region in 750−900 nm appeared due to transition from $^6A_1(^6S)$ to $^4T_1(^4G)$ at 900 nm, which is, however, beyond the wavelength region studied presently.

At room temperature, molecules have many excited states due to vibration and rotation. These states' (rotation and vibration) energy levels are overlaid on the electronic energy levels because they are very closely spaced and have a much smaller energy difference than the electronic energy levels. Thus, an electronic energy level consists of several vibrational and rotational energy levels. So, a molecule has the ability to both absorb energy and experience vibrational−rotational and electronic excitations simultaneously. The simultaneous change in vibrational and rotational states that occurs when an electron moves from one energy level to another leads to transitions between different vibrational and rotational levels of electronic states with varying energies. Therefore, the absorption of many radiations at closely spaced frequencies results in the production of a wide absorption band, as is seen in the present study. The structure and size of the nanoparticles considerably change these outcomes.[53]

The absorption edges (λ_{edge}) and corresponding energy band gaps for FO-O2 and Fe-A2 were determined using the direct formula[54]

$$E_g = \frac{hc}{\lambda_{edge}} = \frac{1240}{\lambda_{edge}} \quad (2a)$$

Table 3. Energy Band Gap (E_g) Values Obtained from Absorption Spectra and Tauc's Plot, and Urbach Energy (E_u) for FO-O2, FO-A2, and FO-N2 Samples

	E_g from eq 2a		E_g from eq 2b		
material	λ_{edge} (nm)	direct band gap (eV)	direct band gap (eV)	indirect band gap (eV)	E_u from eq 3 (eV)
FO-O2	622	1.99	2.01	1.63	0.30
FO-A2	637	1.94	1.96	1.39	0.66
FO-N2	772	1.60	1.46	–	–

and recorded in Table 3. However, Tauc's plot is a well-known technique to estimate the direct and indirect band gap energy:[12]

$$(\alpha h\nu)^n = A(h\nu - E_g) \quad (2b)$$

where α is the absorption coefficient, A is a constant, $h\nu$ is the energy of photon, and n is a constant depending on the nature of the electron transition (n = 2 and n = 1/2 for direct and indirect band gaps, respectively). Figure 4b,c illustrates the $(\alpha h\nu)^2$ vs $h\nu$ and $(\alpha h\nu)^{1/2}$ vs $h\nu$ plots. The intersection of the linear absorption edge component with the energy axis can be used to determine the energy gap. Thus, estimated direct and indirect energy band gap values for FO-O2 and FO-A2 are listed in Table 3 which lie within the range of reported values for hematite (i.e., for direct band gap 1.95−2.35 eV[52] and for indirect energy band gap 1.38−2.09 eV).[55] The determined band gap energy values for FO-O2 and FO-A2 bear an inverse relationship with the particle size, which is in agreement with theoretical predictions for semiconductor nanoparticles.[56]

Figure 5a elucidates the observed UV−vis spectra for FO-N2. The energy band gap calculated using eq 2a is 1.6 eV, whereas using Tauc's plot (see Figure 5b) the calculated direct band gap value for FO-N2 is 1.46 eV; but the indirect band gap for FO-N2, if any, could not be estimated. Though there are several reports on the synthesis and characterization of cementite, optical absorption studies on cementite is rare. Fresno et al.[57] reported a UV−vis absorption spectrum for Fe_3C quite similar to the present one. For nitrogen-doped Fe_3C, Yang et al.[58] estimated the direct band gap energy of 1.65 eV from UV−vis absorption spectra.

Hematite's band gap contains localized defect states, which are the cause for the band gap lowering in FO-O2 and FO-A2 samples. An absorption tail that extends deep into the forbidden gap due to localized defect states is called an Urbach tail, and the associated energy is called Urbach energy.[59] Urbach energy (E_u), defined as the difference between the maximum tailing in the valence band and minimum tailing in the conduction band and physically representing the minimum exciton energy (energy required to separate the hole and electron), describes the role of defects in the material. The electron transition between localized states, whose density depends exponentially on the incident photon energy, is thought to be the source of the band tails width associated with the valence and conduction bands.[60] In the low photon energy range, the UV−vis absorption data are used to calculate the Urbach energy for semiconductors following mathematical relation[60]

$$\alpha = \alpha_0 \exp\left(\frac{h\nu}{E_u}\right) \quad (3)$$

where α = absorption coefficient, α_0 = constant, and $h\nu$ = photon energy. Figure 6 illustrates the lnα vs $h\nu$ plot, where the reciprocal of the slope gives the E_u value. The estimated values of E_u for FO-O2 and FO-A2 samples are 0.30 and 0.66 eV, respectively. An inverse relation between the energy band gap and Urbach energy is noticed for FO-O2 and FO-A2 samples. Thus, a decrease in the optical energy band gap corresponds to an increase of disorder.[61] The higher Urbach energy for FO-A2 than FO-O2 indicates higher density of defect states in FO-A2, an observation that is in agreement with earlier reports.[61,62]

In bulk hematite, photoluminescence transitions are prohibited as a result of the localized d−d transition, effective magnetic relaxation, and resonant energy transfer between cations.[50] Hematite nanostructures, on the other hand, exhibit photoluminescence due to self-trapped states linked to their optical characteristics. In nanodomains, quantum confinement plays an important role in luminescence. It significantly influences the relaxation of the forbidden d−d transitions by

https://doi.org/10.1021/acsomega.3c10332
ACS Omega 2024, 9, 22607−22618

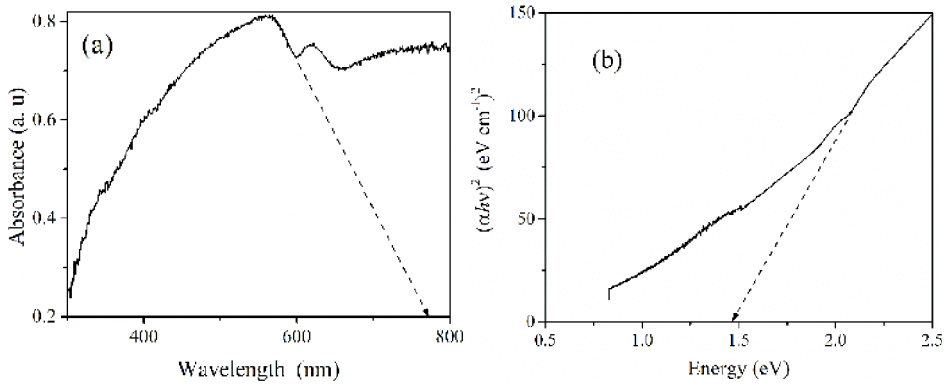

Figure 5. (a) UV−vis spectra of FO-N2; (b) Tauc's plots for n = 2. Dashed lines are guides for the eyes.

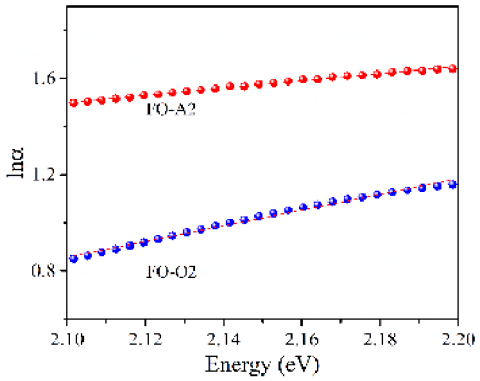

Figure 6. lnα vs photon energy plots to determine the Urbach energy for FO-O2 and FO-A2 samples.

delocalization of the electronic states and quantification of the energy levels. Furthermore, the reduction in particle size affects the long-range magnetic order, which eventually reduces the magnetic interactions between the cations. As a result, long-lived-excited states may emit light after photoexcitation.[63,64]

The room temperature PL spectrum for FO-O2 and FO-A2 samples excited with 532 nm radiation when deconvolved using a Gaussian distribution resolves into two peaks (Figure 7). The deconvoluted spectra displayed broad emission bands with centers at 753 nm (1.64 eV) and 896 nm (1.38 eV) for FO-O2, and 779 nm (1.59 eV) and 916 nm (1.35 eV) for FO-A2. These are consistent with the absorption bands in the near-infrared range for hematite.[65] As seen in other semiconductor nanoparticles, a substantial Stokes shift of the emission peak in comparison to the excitation wavelength can be observed, which can be related to bound-exciton emission.[52] Additionally, redshift of emission band can be observed in larger size nanoparticles due to a decrease in nearby covalency as a result of reduced Racah parameters compared to the small hematite nanoparticles.[47,65] Conversely, the room temperature PL study for the FO-N2 sample when excited with 532 nm radiation did not show any luminescence in the working range of wavelength.[66] Thus, the room temperature PL spectrum for this sample was obtained under excitation of 350 nm radiation, and the deconvoluted spectrum displayed three emission bands with centers at 421, 517, and 613 nm. The relatively less intense and sharper peak at 421 nm may be assigned to the near-band-edge emission, while the broader peaks can be corelated to the surface defects. There are no reports on the PL study on cementite found in the literature.

Apart from the band edge emission, the presence of potential defect levels causes PL emission bands in the prohibited energy region.[67] As the nanoparticles have a high surface-to-volume ratio and short-range ordering, the large surface area often results in an abundance of surface dangling bonds and thereby defect levels, and hence, the prohibited energy gap below the conduction band is filled with donor states. Thus, due to transitions of trapped electrons in various defect states, nonradiative peaks appear in the nanomaterials.[68] Though assignment of the two defect levels corresponding to 1.59−1.64 and 1.35−1.38 eV for the synthesized hematite nanomaterials (FO-O2, and FO-A2) can be easily visualized, the same for FO-N2 will not be straightforward as it has few components.

Raman spectra of iron oxides having several phases show distinctive phonon modes, verifying the purity and type of the

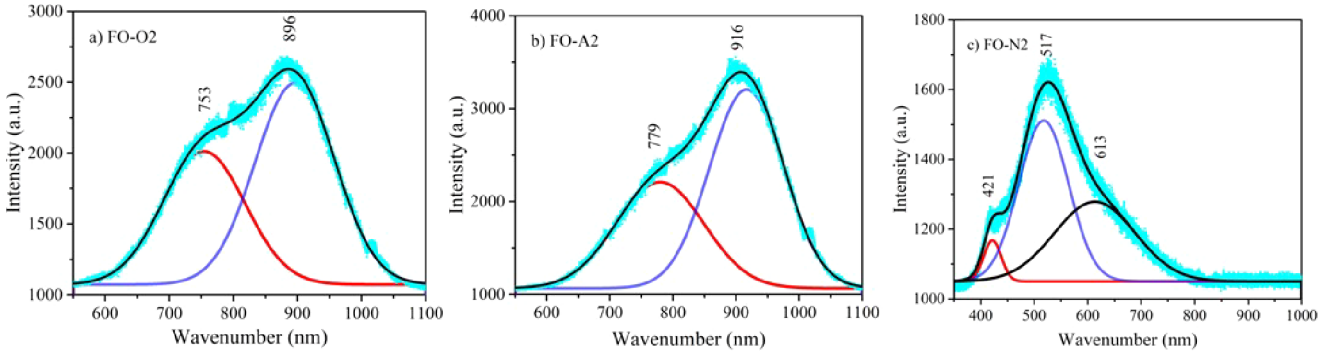

Figure 7. Room temperature photoluminescence (PL) spectra of (a) FO-O2, (b) FO-A2, and (c) FO-N2 samples.

https://doi.org/10.1021/acsomega.3c10332
ACS Omega 2024, 9, 22607−22618

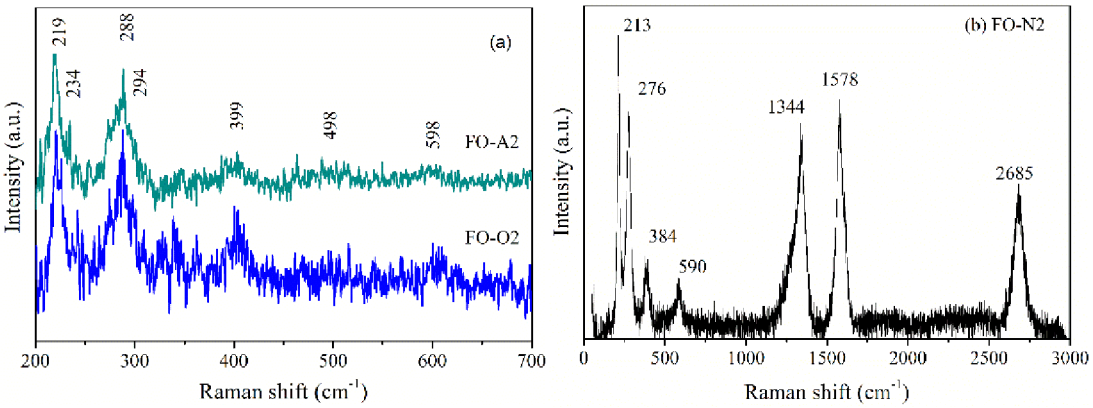

Figure 8. Raman spectra of FO-O2, FO-A2 (a), and FO-N2 (b).

phases.[69] Based on hematite's crystallographic properties, Raman active vibrational modes are represented by[70] $\Gamma_{hematite} = 2A_{1g} + 5E_g$, where seven Raman modes can be experimentally observed.[12] The rhombohedral structure of hematite can be demonstrated analyzing the Raman spectrum. The Raman spectra of hematite samples (FO-O2 and FO-A2) recorded at room temperature in the range of 100 to 700 cm^{-1} are illustrated in Figure 8. Significant bands can be seen in each spectrum where the bands appearing at 219 and 498 cm^{-1} are assigned to A_{1g} and bands at 234, 288, 294, 399, 598 cm^{-1} are attributed to E_g.[12] The strongest bands are found at 219 and 288 cm^{-1}, whereas the weakest band appears at 498 cm^{-1}. Low-frequency modes (200−300 cm^{-1}) have been assigned to Fe atom vibrations, whereas O atom vibrations have been responsible for the bands in the range 400−650 cm^{-1}. It is believed that the A_{1g} band at 219 cm^{-1} is caused by the migration of iron cations along the *c*-axis. The symmetric mode of O atoms with respect to other cations in a plane perpendicular to the crystallographic *c*-axis and Fe−O stretching vibrations, are attributed to the E_g bands at 399 and 598 cm^{-1}, respectively.[71] These findings further confirm that the FO-O2 and FO-A2 samples are pure hematite. No additional iron oxide, such as magnetite or maghemite, was found, proving the high degree of purity of the products. There have been reports of similar outcomes for hematite nanoparticles.[12,72,73]

Less information is available in the literature on the Raman study of pure iron carbide. The Raman spectrum of FO-N2 (Figure 8) displays five prominent peaks at 213, 276, 1328, 1588, and 2685 cm^{-1} along with two weak peaks at 384 and 590 cm^{-1}. In general, bulk iron carbide is often Raman inactive because of its metallic nature.[74−76] The peaks observed between 200 and 600 cm^{-1} range in the spectrum of FO-N2 are similar to those reported for Fe_3C-based nanostructures[75] and $LiFePO_4$/C composite,[27] and thus likewise the peaks in the 200 and 600 cm^{-1} range can be allotted to Fe_3C present in FO-N2 representing the stretching modes between the iron and carbon atoms, confirming the formation of Fe_3C nanoparticles. The formation of Fe_3C was observed from the pyrolysis of ferrocene or ferrocene/hydrocarbon mixtures in previous studies.[23−27] The two prominent peaks observed at 1328 and 1588 cm^{-1} for FO-N2 correspond to the so-called D and G characteristic carbon peaks.[27,75−79] This indicates that FO-N2 contains amorphous carbon content possibly with graphitic and glassy nanostructures, which could not be detected by the XRD analysis. In the Raman spectrum of FO-N2, one overtone of D band was also seen at 2685 cm^{-1}.

2.3. Thermal Decomposition Reactions. Now, based on literature, we attempt to propose the reactions that took place during the thermal conversion of ferrocene in the presence of oxalic acid dihydrate carried out in different reaction atmospheres. As stated earlier[32,33,35,37] solid ferrocene thermally decomposes (sublimates) at 453 K and above 773 K ferrocene vapor decomposes to metallic iron and some gaseous products

$$(C_5H_5)_2Fe \rightarrow Fe + H_2(g) + CH_4(g) + C_5H_6(g) + \ldots$$

whereas above 373 K bare oxalic acid dihydrate decomposes as

$$(COOH)_2 \cdot 2H_2O \rightarrow CO_2(g) + CO(g) + H_2O(g)$$

Presently, the overall thermal reaction of ferrocene in the presence of oxalic acid dihydrate in O_2 and air atmospheres may be assumed[29] as follows

$$2[(C_5H_5)_2Fe] + (COOH)_2 \cdot 2H_2O \rightarrow Fe_2O_3(s) + CO_2(g) + CO(g) + 13H_2(g) + 20C$$

where metallic iron deoxidized the CO_2 and/or CO to produce oxygen and carbon[80] and then reacted with the available oxygen to form hematite (α-Fe_2O_3). As per literature,[81,82] α-Fe_2O_3 under N_2 atmosphere may convert to cementite (Fe_3C) as follows:

$$3Fe_2O_3 + 5H_2 + 2CH_4 = 2Fe_3C + 9H_2O^{82}$$

$$3Fe_2O_3 + 13H_2 + 2CO_2 = 2Fe_3C + 13H_2O^{83}$$

Thus, it may be inferred that during thermal decomposition of ferrocene and oxalic acid dihydrate mixture in O_2 and air atmospheres, pure hematite was formed on oxidation of metallic iron in the presence of copious oxygen; however, in N_2 atmosphere the oxygen available from the breaking of oxalic acid dihydrate first led to the formation of hematite, which subsequently was reduced to cementite. Further, it is known that when heated above 600 °C Fe_3C transforms into α-Fe and C.[83,84] Existence of amorphous C has been detected in a Raman study of FO-N2. Thus, it is plausible that during second annealing of Fe-N1, Fe_3C slowly starts the conversion making Fe-N2 a mixture of Fe_3C and α-Fe. This gives a clue to prepare pure Fe_3C from ferrocene and oxalic acid mixture in N_2 atmosphere.

https://doi.org/10.1021/acsomega.3c10332
ACS Omega 2024, 9, 22607−22618

Table 4. Different Conditions of Material Preparation

	as grown			1st annealed			2nd annealed		
reaction environment	T (°C)	time (min)	sample name	T (°C)	time (h)	sample name	T (°C)	time (h)	sample name
O_2	500	∼55	FO-O	500	2	FO-O1	750	2	FO-O2
Air	300	∼30	FO-A	300	2	FO-A1	750	2	FO-A2
N_2	300	∼30	FO-N	300	2	FO-N1	750	2	FO-N2

3. CONCLUSIONS

The present study demonstrates the solid-state synthesis of hematite and cementite nanostructures through the thermal decomposition of ferrocene in the presence of oxalic acid dihydrate as a coprecursor as evident from XRD results. Satisfactory crystallinity was obtained on repeated annealing at 750 °C. Physical techniques like Rietveld refinement of XRD data, absorption, and Raman spectroscopy were employed to identify the phase of the synthesized materials. The results showed that hematite nanostructures were formed in oxidative and ambient atmospheres, while mainly cementite was found in an inert atmosphere. Particle size of the synthesized materials was estimated using Scherer and Halder−Wagner methods, which was in close agreement with those observed in the particle size histogram obtained from FE-SEM and TEM images. The elemental composition of each material was revealed by EDX analysis. Optical band gaps of the powdery materials were calculated using absorption band edge and Tauc's plot technique. For hematite materials, different electronic transitions occurred between the $3d^5$ shell of the octahedrally coordinated Fe^{3+} ions that caused the optical absorption were identified. Urbach energy was estimated, which described the role of defects in the synthesized hematite. The nanomaterials exhibited photoluminescence as a result of self-trapped states linked to their optical characteristics. For hematite, seven Raman modes ($2A_{1g} + 5E_g$) could be experimentally observed confirming the rhombohedral structure. On the other hand, for cementite the D and G bands were clearly visible in the Raman spectra. A plausible analysis of the undergoing solid-state reactions has been provided. Overall, this study provides valuable insights into the role of reaction atmosphere on the thermal decomposition of ferrocene in the presence of oxalic acid dihydrate leading to hematite and cementite nanomaterials.

4. EXPERIMENTAL AND ANALYTICAL METHODS

Ferrocene and oxalic acid dihydrate obtained from Sigma-Aldrich and Merck, respectively, were employed without additional purification. Using an agate mortar, a fine solid mixture of ferrocene (precursor) and oxalic acid dihydrate (coprecursor) was prepared in a 1:1 weight ratio. The solid-state reaction of the mixture was performed using alumina made crucibles (i) in an indigenous furnace in air atmosphere and (ii) inside a thermogravimetric analyzer, TGA (model no. STA 449 F3 Jupiter, Netzsch, Germany) in UHP (99.999%) O_2 and UHP (99.999%) N_2 dynamic gas atmospheres.

Powder XRD patterns of the as-grown samples (FO-O, FO-A, FO-N) collected just after the thermal decomposition were analyzed with a Rigaku Smart Lab X-ray diffractometer with Cu-K_α (λ = 1.5405 nm); however, it was noticed from the observed XRD patterns that those samples were not in perfectly crystalline phase. Then the decomposed samples were annealed in respective gaseous environments and at 500 °C for 2 h.; XRD study of the first annealed samples (FO-O1, FO-A1, FO-N1) also did not exhibit perfect crystalline phases. So, this led to further annealing of FO-O1, FO-A1, and FO-N1 samples for another 2 h at 750 °C. The materials thus obtained, FO-O2, FO-A2, and FO-N2, exhibited perfect crystalline phases and were used for further characterization studies. The sample preparation conditions are listed in Table 4. In comparison to the starting amount, the yield for FO-O2, FO-A2, and FO-N2 are 5.8%, 4.2%, and 3.1%, respectively. FE-SEM images were obtained using ZEISS Gemini instrument with 30 kV accelerating voltage. Atomic percentage and elemental information from EDX were collected using Octane Elect EDS system with Silicon Drift Detector (SDD) technology attached to the FE-SEM system and using analysis APEX software. High-resolution transmission electron microscope (HR-TEM) images were captured with the JEM-F200 F2Multipurpose Analytical S/TEM and TECNAI G2 TF20-ST. A Cary-5000 UV−vis−NIR spectrometer was used to collect the absorption spectra of these samples in diffused reflectance spectra (DRS) mode. The photoluminescence (PL) and Raman spectra were taken with the help of HORIBA Scientific's Confocal Raman Microscope (Lab RAM HR Evolution).

AUTHOR INFORMATION

Corresponding Author

Ashis Bhattacharjee − *Department of Physics, Visva-Bharati University, Santiniketan 731235, India;* orcid.org/0000-0002-0180-409X; Email: ashis.bhattacharjee@visva-bharati.ac.in

Authors

Sani Kundu − *Department of Physics, Visva-Bharati University, Santiniketan 731235, India*

Toton Sarkar − *Department of Physics, Visva-Bharati University, Santiniketan 731235, India*

Gurupada Ghorai − *School of Physical Sciences, An OCC of Homi Bhabha National Institute, National Institute of Science Education and Research, Jatni, Odisha 752050, India;* orcid.org/0000-0001-9410-6022

Pratap K. Sahoo − *School of Physical Sciences, An OCC of Homi Bhabha National Institute, National Institute of Science Education and Research, Jatni, Odisha 752050, India;* orcid.org/0000-0003-1448-6008

Ahmad Aziz Al-Ahmadi − *Department of Electrical Engineering, College of Engineering, Taif University, Taif 21944, Saudi Arabia*

Ahmad Alghamdi − *Department of Mechanical and Industrial Engineering, College of Engineering and Computing in Al-Qunfudhah, Umm al-Qura University, Mecca 21955, Saudi Arabia*

Complete contact information is available at: https://pubs.acs.org/10.1021/acsomega.3c10332

https://doi.org/10.1021/acsomega.3c10332
ACS Omega 2024, 9, 22607−22618

Author Contributions

Material preparation, major data collection, and analysis were performed by S.K. T.S, G.G., and P.K.S. were involved in some data collections, while A.A.A. and A.A. were involved in data curation. A.B. conceptualized the problem and designed the study. The first draft of the manuscript was written by S.K. and finalized by A.B. Authors reviewed the final manuscript.

Notes

The authors declare no competing financial interest.

■ ACKNOWLEDGMENTS

Author S.K. is thankful to DST-INSPIRE, Govt of India for providing a fellowship. The financial support for the thermogravimetry analyzer from the Department of Science and Technology (DST), Govt. of India through a grant (ref. no. SR/FIST/PSI-157/2010) to the Department of Physics, Visva-Bharati University is gratefully acknowledged. The authors A.A.A. and A.A. extend their appreciation to Taif University, Saudi Arabia, for supporting this work through the project number (TU-DSPP-2024-56).

■ REFERENCES

(1) Alinezhad, H.; Amiri, P. H. T.; Tavakkoli, S. M.; Muhiebes, R. M.; Mustafa, Y. F. Progressive Types of Fe_3O_4 Nanoparticles and their Hybrids as Catalysts. *J. Chem. Rev* **2022**, *4* (4), 288−312.

(2) Vermisoglou, E. C.; Devlin, E.; Giannakopoulou, T.; Romanos, G.; Boukos, N.; Psycharis, V.; Lei, C.; Lekakou, C.; Petridis, D.; Trapalis, C. Reduced Graphene Oxide/Iron Carbide Nanocomposites for Magnetic and Supercapacitor Applications. *J. Alloys Compd.* **2014**, *590*, 102−109.

(3) Bordet, A.; Landis, R. F.; Lee, Y.; Tonga, G. Y.; Asensio, J. M.; Li, C.-H.; Fazzini, P.-F.; Soulantica, K.; Rotello, V. M.; Chaudret, B. Water-Dispersible and Biocompatible Iron Carbide Nanoparticles with High Specific Absorption Rate. *ACS Nano* **2019**, *13* (3), 2870−2878.

(4) Sangaiya, P.; Jayaprakash, R. A Review on Iron Oxide Nanoparticles and their Biomedical Applications. *J. Supercond. Novel Magn.* **2018**, *31* (11), 3397−3413.

(5) Wang, J.; Hou, Y. Iron Carbide Nanostructures: An Emerging Material for Tumor Theranostics. *Acc. Mater. Res.* **2022**, *3* (1), 89−99.

(6) Wu, W.; Wu, Z.; Yu, T.; Jiang, C.; Kim, W.-S. Recent Progress on Magnetic Iron Oxide Nanoparticles: Synthesis, Surface Functional Strategies and Biomedical Applications. *Sci. Technol. Adv. Mater.* **2015**, *16* (2), 23501.

(7) Long, N. V.; Teranishi, T.; Yang, Y.; Thi, C. M.; Cao, Y.; Nogami, M. Iron Oxide Nanoparticles for next Generation Gas Sensors. *Int J. Metall. Mater. Eng.* **2015**, *1* (2), 2455−2372.

(8) Lemine, O. M.; Madkhali, N.; Hjiri, M.; All, N. A.; Aida, M. S. Comparative Heating Efficiency of Hematite (α-Fe2O3) and Nickel Ferrite Nanoparticles for Magnetic Hyperthermia Application. *Ceram. Int.* **2020**, *46* (18), 28821−28827.

(9) Gul, S.; Khan, S. B.; Rehman, I. U.; Khan, M. A.; Khan, M. I. A Comprehensive Review of Magnetic Nanomaterials Modern Day Theranostics. *Front. Mater.* **2019**, *6*, 179.

(10) Nikitin, A. A.; Shchetinin, I. V.; Tabachkova, N. Y.; Soldatov, M. A.; Soldatov, A. V.; Sviridenkova, N. V.; Beloglazkina, E. K.; Savchenko, A. G.; Fedorova, N. D.; Abakumov, M. A. Synthesis of Iron Oxide Nanoclusters by Thermal Decomposition. *Langmuir* **2018**, *34* (15), 4640−4650.

(11) Kumar, S.; Kumar, M.; Singh, A. Synthesis and Characterization of Iron Oxide Nanoparticles (Fe_2O_3, Fe_3O_4): A Brief Review. *Contemp. Biophys.* **2021**, *62* (3), 144−164.

(12) Kundu, S.; Sarkar, T.; Ghorai, G.; Zubko, M.; Sahoo, P. K.; Weselski, M.; Reddy, V. R.; Bhattacharjee, A. Study on Co-Precursor Driven Solid State Thermal Conversion of Iron(III)Citrate to Iron Oxide Nanomaterials. *Appl. Phys. A: Mater. Sci. Process.* **2023**, *129* (4), 264.

(13) Meffre, A.; Mehdaoui, B.; Kelsen, V.; Fazzini, P. F.; Carrey, J.; Lachaize, S.; Respaud, M.; Chaudret, B. A Simple Chemical Route toward Monodisperse Iron Carbide Nanoparticles Displaying Tunable Magnetic and Unprecedented Hyperthermia Properties. *Nano Lett.* **2012**, *12* (9), 4722−4728.

(14) Wang, X.; Zhu, K.; Ju, Y.; Li, Y.; Li, W.; Xu, J.; Hou, Y. Iron Carbides: Magic Materials with Magnetic and Catalytic Properties. *J. Magn. Magn. Mater.* **2019**, *489*, 165432.

(15) Han, J.; Kim, K.; Tavakkoli, M.; Lee, J.; Kim, D.; Chung, I.; Lee, A.; Park, K.; Liao, Y.; Lee, J. M.; et al.et al. Upcycled Synthesis and Extraction of Carbon-encapsulated Iron Carbide Nanoparticles for Gap Plasmon Applications in Perovskite Solar Cells. *EcoMat* **2023**, *5* (6), No. e12342.

(16) Khurshid, H.; Abdu, Y. A.; Devlin, E.; Issa, B. A.; Hadjipanayis, G. C. Chemically Synthesized Nanoparticles of Iron and Iron-Carbides. *RSC Adv.* **2020**, *10* (48), 28958−28964.

(17) Abel, F. M.; Pourmiri, S.; Basina, G.; Tzitzios, V.; Devlin, E.; Hadjipanayis, G. C. Iron Carbide Nanoplatelets: Colloidal Synthesis and Characterization. *Nanoscale Adv.* **2019**, *1* (11), 4476−4480.

(18) Astruc, D. Why Is Ferrocene so Exceptional? *Eur. J. Inorg. Chem.* **2017**, *2017* (1), 6−29.

(19) Amara, D.; Margel, S. Synthesis and Characterization of Elemental Iron and Iron Oxide Nano/Microcomposite Particles by Thermal Decomposition of Ferrocene. *Nanotechnol. Rev.* **2013**, *2* (3), 333−357.

(20) Lobo Guerrero, A.; Rebollo-Plata, B.; Gallegos, J. H. G.; Uribe, D. B.; Altamirano, M. A. G.; Cabal-Velarde, J. G. Study of Bamboo-Type Carbon Nanotubes with Magnetic Iron Carbide Nanoparticles Fabricated by a Modified CVD Method. *J. Nanopart. Res.* **2021**, *23*, 1−10.

(21) Zhigach, A. N.; Leipunsky, I. O.; Kuskov, M. L.; Berezkina, N. G.; Afanasenkova, E. S.; Lopez, G. W.; Skryleva, E. A.; Menushenkov, V. P.; Zhigalina, O. M.; Khmelenin, D. N. On the Production of Dispersive Single-Crystal Iron Carbide (Fe3C) Nanoparticulate. *Bull. Mater. Sci.* **2022**, *45* (1), 38.

(22) Kumar, R.; Sahoo, B. One-Step Pyrolytic Synthesis and Growth Mechanism of Core−Shell Type Fe/Fe3C-Graphite Nanoparticles-Embedded Carbon Globules. *Nano-Struct. Nano-Objects* **2018**, *16*, 77−85.

(23) Zhang, C.; Tian, B.; Chong, C. T.; Ding, B.; Fan, L.; Chang, X.; Hochgreb, S. Experimental Study of Thiophene and Ferrocene in Synthesis of Single-Walled Carbon Nanotubes in Rich Premixed Hydrogen/Air Flames. *Combust. Flame* **2022**, *238*, 111939.

(24) Lyubutin, I. S.; Anosova, O. A.; Frolov, K. V.; Sulyanov, S. N.; Okotrub, A. V.; Kudashov, A. G.; Bulusheva, L. G. Iron Nanoparticles in Aligned Arrays of Pure and Nitrogen-Doped Carbon Nanotubes. *Carbon* **2012**, *50* (7), 2628−2634.

(25) Chaiwat, W.; Kaewtrakulchai, N.; Sangsiri, P.; Eiad-Ua, A.; Wongwiriyapan, W.; Viriya-Empikul, N.; Suttiponpanit, K.; Charinpanitkul, T. Dependence of MWCNT Production via Co-Pyrolysis of Industrial Slop Oil and Ferrocene on Growth Temperature and Heating Rate. *J. Anal. Appl. Pyrolysis* **2020**, *150*, 104878.

(26) Andrews, R.; Jacques, D.; Rao, A. M.; Derbyshire, F.; Qian, D.; Fan, X.; Dickey, E. C.; Chen, J. Continuous Production of Aligned Carbon Nanotubes: A Step Closer to Commercial Realization. *Chem. Phys. Lett.* **1999**, *303* (5−6), 467−474.

(27) Doeff, M. M.; Wilcox, J. D.; Yu, R.; Aumentado, A.; Marcinek, M.; Kostecki, R. Impact of Carbon Structure and Morphology on the Electrochemical Performance of LiFePO 4/C Composites. *J. Solid State Electrochem.* **2008**, *12*, 995−1001.

(28) Koprinarov, N.; Konstantinova, M.; Marinov, M. Ferromagnetic Nanomaterials Obtained by Thermal Decomposition of Ferrocene. *Solid State Phenom.* **2010**, *159*, 105−108.

(29) Bhattacharjee, A.; Rooj, A.; Roy, M.; Kusz, J.; Gütlich, P. Solventless Synthesis of Hematite Nanoparticles Using Ferrocene. *J. Mater. Sci.* **2013**, *48* (7), 2961−2968.

https://doi.org/10.1021/acsomega.3c10332
ACS Omega 2024, 9, 22607−22618

(30) Sajitha, E. P.; Prasad, V.; Subramanyam, S. V.; Mishra, A. K.; Sarkar, S.; Bansal, C. Size-Dependent Magnetic Properties of Iron Carbide Nanoparticles Embedded in a Carbon Matrix. *J. Phys.: Condens. Matter* **2007**, *19* (4), 046214.
(31) Kumari, R.; Krishnia, L.; Kumar, V.; Singh, S.; Singh, H. K.; Kotnala, R. K.; Juluri, R. R.; Bhatta, U. M.; Satyam, P. V.; Yadav, B. S. Fe 3 C-Filled Carbon Nanotubes: Permanent Cylindrical Nanomagnets Possessing Exotic Magnetic Properties. *Nanoscale* **2016**, *8* (7), 4299−4310.
(32) Bhattacharjee, A.; Rooj, A.; Roy, D.; Roy, M. Thermal Decomposition Study of Ferrocene $[(C_5H_5)_2Fe]$. *J. Exp. Phys.* **2014**, *2014*, 513268.
(33) Leonhardt, A.; Hampel, S.; Müller, C.; Mönch, I.; Koseva, R.; Ritschel, M.; Elefant, D.; Biedermann, K.; Büchner, B. Synthesis, Properties, and Applications of Ferromagnetic-Filled Carbon Nanotubes. *Chem. Vap. Deposition* **2006**, *12* (6), 380−387.
(34) Rooj, A.; Roy, M.; Bhattacharjee, A. Investigation on the Thermal Decomposition of Ferrocene in Diffirent Reaction Atmospheres. *Thesis*, Visva Bharti University, 2016.
(35) Lapidus, G.; Barton, D.; Yankwich, P. E. Kinetics and Stoichiometry of the Gas-Phase Decomposition of Oxalic Acid. *J. Phys. Chem.* **1964**, *68* (7), 1863−1865.
(36) Rahman, M. M.; Khan, S. B.; Jamal, A.; Faisal, M.; Aisiri, A. M. Iron Oxide Nanoparticles. *Nanomaterials* **2011**, *3*, 43−67.
(37) Kundu, S.; Chakraborty, M.; Bhattacharjee, A. Solid-State Reaction of Ferrocene Controlled by Co-Precursor and Reaction Atmosphere Leading to Hematite and Cohenite Nanomaterials: A Reaction Kinetic Study. *J. Phys. Chem. C* **2023**, *127* (37), 18397−18408.
(38) Kundu, S.; Chakraborty, M.; Bhattacharjee, A. Correction to "Solid-State Reaction of Ferrocene Controlled by Co-Precursor and Reaction Atmosphere Leading to Hematite and Cohenite Nanomaterials: A Reaction Kinetic Study. *J. Phys. Chem. C* **2023**, *127*, 18397.
(39) Cullity, B. D.; Stock, S. R. *Elements of X-Ray Diffraction*, 3rd, Ed.; Prentice Hall: New York, pp 174177; 2001.
(40) Basak, M.; Rahman, M. L.; Ahmed, M. F.; Biswas, B.; Sharmin, N. The Use of X-Ray Diffraction Peak Profile Analysis to Determine the Structural Parameters of Cobalt Ferrite Nanoparticles Using Debye-Scherrer, Williamson-Hall, Halder-Wagner and Size-Strain Plot: Different Precipitating Agent Approach. *J. Alloys Compd.* **2022**, *895*, 162694.
(41) Jahil, S.; Mohammed, I.; Khazaal, A.; Jasim, K.; Harbbi, K. Application the Halder − Wagner to Calculation Crystal Size and Micro Strain by X-ray Diffraction Peaks Analysis. *NeuroQuantology* **2022**, *20*, 199−204.
(42) Sen, S. K.; Barman, U. C.; Manir, M. S.; Mondal, P.; Dutta, S.; Paul, M.; Chowdhury, M. A. M.; Hakim, M. A. X-Ray Peak Profile Analysis of Pure and Dy-Doped α-MoO3 Nanobelts Using Debye-Scherrer, Williamson-Hall and Halder-Wagner Methods. *Adv. Nat. Sci.: Nanosci. Nanotechnol.* **2020**, *11* (2), 25004.
(43) Sarkar, T.; Kundu, S.; Ghorai, G.; Sahoo, P. K.; Bhattacharjee, A. Structural, Spectroscopic and Morphology Studies on Green Synthesized ZnO Nanoparticles. *Adv. Nat. Sci.: Nanosci. Nanotechnol.* **2023**, *14* (3), 35001.
(44) Maji, S. K.; Mukherjee, N.; Mondal, A.; Adhikary, B. S. Synthesis, characterization and photocatalytic activity of α-Fe_2O_3 nanoparticles. *Polyhedron* **2012**, *33* (1), 145−149.
(45) Dash, P.; Pattanayak, S.; Majhi, M.; Nayak, B. Facile and Controllable Synthesis of Hematite (α-Fe_2O_3) Nanostructures Using GRA-APSO and ANN: Reaction Performance Optimization for Haemotoxicity and MRI Assessment. *J. Alloys Compd.* **2023**, *957*, 170383.
(46) Konicki, W.; Pełech, I.; Mijowska, E.; Jasińska, I. Adsorption of Anionic Dye Direct Red 23 onto Magnetic Multi-Walled Carbon Nanotubes-Fe3C Nanocomposite: Kinetics, Equilibrium and Thermodynamics. *Chem. Eng. J.* **2012**, *210*, 87−95.
(47) Sherman, D. M.; Waite, T. D. Electronic Spectra of Fe3+ Oxides and Oxide Hydroxides in the near IR to near UV. *Am. Mineral.* **1985**, *70* (11−12), 1262−1269.
(48) Rufus, A.; Sreeju, N.; Vilas, V.; Philip, D. Biosynthesis of Hematite (α-Fe2O3) Nanostructures: Size Effects on Applications in Thermal Conductivity, Catalysis, and Antibacterial Activity. *J. Mol. Liq.* **2017**, *242*, 537−549.
(49) He, Y. P.; Miao, Y. M.; Li, C. R.; Wang, S. Q.; Cao, L.; Xie, S. S.; Yang, G. Z.; Zou, B. S.; Burda, C. Size and Structure Effect on Optical Transitions of Iron Oxide Nanocrystals. *Phys. Rev. B* **2005**, *71* (12), 125411.
(50) Wheeler, D. A.; Wang, G.; Ling, Y.; Li, Y.; Zhang, J. Z. Nanostructured Hematite: Synthesis, Characterization, Charge Carrier Dynamics, and Photoelectrochemical Properties. *Energy Environ. Sci.* **2012**, *5* (5), 6682−6702.
(51) Mitra, S.; Das, S.; Mandal, K.; Chaudhuri, S. Synthesis of a α-Fe2O3 Nanocrystal in Its Different Morphological Attributes: Growth Mechanism, Optical and Magnetic Properties. *Nanotechnology* **2007**, *18* (27), 275608.
(52) Rufus, A.; Sreeju, N.; Philip, D. Synthesis of Biogenic Hematite (α-Fe_2O_3) Nanoparticles for Antibacterial and Nanofluid Applications. *RSC Adv.* **2016**, *6* (96), 94206−94217.
(53) Rufus, A.; Sreeju, N.; Philip, D. Size Tunable Biosynthesis and Luminescence Quenching of Nanostructured Hematite (α-Fe_2O_3) for Catalytic Degradation of Organic Pollutants. *J. Phys. Chem. Solids* **2019**, *124*, 221−234.
(54) Baset, S.; Akbari, H.; Zeynali, H.; Shafie, M. Size Measurement of Metal and Semiconductor Nanoparticles via UV-Vis Absorption Spectra. *Dig. J. Nanomater. Biostructures* **2011**, *6* (2), 709−716.
(55) Özer, N.; Tepehan, F. Optical and Electrochemical Characteristics of Sol−Gel Deposited Iron Oxide Films. *Sol. Energy Mater. Sol. Cells* **1999**, *56* (2), 141−152.
(56) Singh, M.; Taele, B. M.; Goyal, M. Modeling of Size and Shape Dependent Band Gap, Dielectric Constant and Phonon Frequency of Semiconductor Nanosolids. *Chin. J. Phys.* **2021**, *70*, 26−36.
(57) Fresno, F.; Iglesias-Juez, A.; Coronado, J. M. Photothermal Catalytic CO_2 Conversion: Beyond Catalysis and Photocatalysis. *Top. Curr. Chem.* **2023**, *381* (4), 21.
(58) Yang, X.; Li, C.; Huang, J.; Liu, Y.; Chen, W.; Shen, J.; Zhu, Y.; Li, C. Nitrogen-Doped Fe_3C@ C Particles as an Efficient Heterogeneous Photo-Assisted Fenton Catalyst. *RSC Adv.* **2017**, *7* (25), 15168−15175.
(59) Boubaker, K. A Physical Explanation to the Controversial Urbach Tailing Universality. *Eur. Phys. J. Plus* **2011**, *126*, 1−4.
(60) Parmar, R.; Kundu, R. S.; Punia, R.; Aghamkar, P.; Kishore, N. Iron Modified Structural and Optical Spectral Properties of Bismuth Silicate Glasses. *Phys. B* **2014**, *450*, 39−44.
(61) Jandow, N. N.; Habubi, N. F.; Al-Baidhany, I. A.; Qaeed, M. A. Annealing Effects on Band Tail Width, Urbach Energy and Optical Parameters of Fe_2O_3: Ni Thin Films Prepared by Chemical Spray Pyrolysis Technique. *Int. J. Nanoelectron. Mater.* **2019**, *12*, 1.
(62) Badawi, A.; Alharthi, S. S.; Alotaibi, A. A.; Althobaiti, M. G. Tailoring the Structural and Optical Characteristics of Hematite (α-Fe2O3) Nanostructures by Barium/Aluminum Dual Doping for Eco-Friendly Applications. *Appl. Phys. A* **2023**, *129* (5), 339.
(63) Zou, B. S.; Volkov, V. Surface Modification on Time-Resolved Fluorescences of Fe_2O_3 Nanocrystals. *J. Phys. Chem. Solids* **2000**, *61* (5), 757−764.
(64) Qureshi, A. A.; Javed, S.; Javed, H. M. A.; Jamshaid, M.; Ali, U.; Akram, M. A. Systematic Investigation of Structural, Morphological, Thermal, Optoelectronic, and Magnetic Properties of High-Purity Hematite/Magnetite Nanoparticles for Optoelectronics. *Nanomaterials* **2022**, *12* (10), 1635.
(65) Zhang, Y.; Liu, W.; Wu, C.; Gong, T.; Wei, J.; Ma, M.; Wang, K.; Zhong, M.; Wu, D. Photoluminescence of Fe2O3 Nanoparticles Prepared by Laser Oxidation of Fe Catalysts in Carbon Nanotubes. *Mater. Res. Bull.* **2008**, *43* (12), 3490−3494.
(66) Irfan, R. M.; Tahir, M. H.; Nadeem, M.; Maqsood, M.; Bashir, T.; Iqbal, S.; Zhao, J.; Gao, L. Fe3C/CdS as Noble-Metal-Free Composite Photocatalyst for Highly Enhanced Photocatalytic H2 Production under Visible Light. *Appl. Catal., A* **2020**, *603*, 117768.

https://doi.org/10.1021/acsomega.3c10332
ACS Omega 2024, 9, 22607−22618

(67) Sadat, M. E.; Kaveh Baghbador, M.; Dunn, A. W.; Wagner, H. P.; Ewing, R. C.; Zhang, J.; Xu, H.; Pauletti, G. M.; Mast, D. B.; Shi, D. Photoluminescence and Photothermal Effect of Fe3O4 Nanoparticles for Medical Imaging and Therapy. *Appl. Phys. Lett.* **2014**, *105* (9), 091903.
(68) Thomas, P.; Sreekanth, P.; Abraham, K. E. Nanosecond and Ultrafast Optical Power Limiting in Luminescent Fe2O3 Hexagonal Nanomorphotype. *J. Appl. Phys.* **2015**, *117* (5), 053103.
(69) Fouad, D. E.; Zhang, C.; El-Didamony, H.; Yingnan, L.; Mekuria, T. D.; Shah, A. H. I. S. Improved size, morphology and crystallinity of hematite (α-Fe2O3) nanoparticles synthesized via the precipitation route using ferric sulfate precursor. *Results Phys.* **2019**, *12*, 1253−1261.
(70) Marshall, C. P.; Dufresne, W. J. B.; Rufledt, C. J. Polarized Raman Spectra of Hematite and Assignment of External Modes. *J. Raman Spectrosc.* **2020**, *51* (9), 1522−1529.
(71) Chernyshova, I. V.; Hochella Jr, M. F.; Madden, A. S. Size-Dependent Structural Transformations of Hematite Nanoparticles. 1. Phase Transition. *Phys. Chem. Chem. Phys.* **2007**, *9* (14), 1736−1750.
(72) Lassoued, A.; Lassoued, M. S.; Dkhil, B.; Ammar, S.; Gadri, A. S. Synthesis, photoluminescence and Magnetic properties of iron oxide (α-Fe2O3) nanoparticles through precipitation or hydrothermal methods. *Phys. E (Amsterdam, Neth.)* **2018**, *101*, 212−219.
(73) Xu, Y. Y.; Zhao, D.; Zhang, X. J.; Jin, W. T.; Kashkarov, P.; Zhang, H. Synthesis and Characterization of Single-Crystalline α-Fe2O3 Nanoleaves. *Phys. E (Amsterdam, Neth.)* **2009**, *41* (5), 806−811.
(74) Park, E.; Ostrovski, O.; Zhang, J.; Thomson, S.; Howe, R. Characterization of Phases Formed in the Iron Carbide Process by X-Ray Diffraction, Mossbauer, X-Ray Photoelectron Spectroscopy, and Raman Spectroscopy Analyses. *Metall. Mater. Trans. B* **2001**, *32* (5), 839−845.
(75) Giordano, C.; Kraupner, A.; Fleischer, I.; Henrich, C.; Klingelhöfer, G.; Antonietti, M. Non-Conventional Fe_3C-Based Nanostructures. *J. Mater. Chem.* **2011**, *21* (42), 16963−16967.
(76) Bi, X.-X.; Ganguly, B.; Huffman, G. P.; Huggins, F. E.; Endo, M.; Eklund, P. C. Nanocrystalline α−Fe, Fe_3C, and Fe_7C_3 Produced by CO_2 Laser Pyrolysis. *J. Mater. Res.* **1993**, *8* (7), 1666−1674.
(77) Wang, X.; Zhang, S.; Li, J.; Xu, J.; Wang, X. Fabrication of Fe/Fe 3 C@ Porous Carbon Sheets from Biomass and Their Application for Simultaneous Reduction and Adsorption of Uranium (VI) from Solution. *Inorg. Chem. Front.* **2014**, *1* (8), 641−648.
(78) Heszler, P.; Elihn, K.; Boman, M.; Carlsson, J.-O. Optical Characterisation of the Photolytic Decomposition of Ferrocene into Nanoparticles. *Appl. Phys. A: Mater. Sci. Process.* **2000**, *70*, 613−616.
(79) Wang, X.; Zhang, P.; Wang, W.; Lei, X.; Zou, B.; Yang, H. Synthesis, Structure and Magnetic Properties of Graphite Carbon Encapsulated Fe_3C Nanoparticles for Applications as Adsorbents. *RSC Adv.* **2015**, *5* (35), 27857−27861.
(80) Qian, W.; Chen, Q.; Cao, F.; Chen, C. Synthesis and Characterization of Polyhedral Graphite Particles. *Open Mater. Sci. J.* **2008**, *2* (1), 19−22.
(81) Nassaralla, C. L. Iron Production. In *Encyclopedia of Materials: Science and Technology*; Elsevier: Oxford; 2001, pp 42964301. DOI: .
(82) Liu, Y.; Murthy, P.; Zhang, X.; Wang, H.; Shi, C. Phase Transformation of Iron Oxide to Carbide and Fe_3C Being Active Centers for RWGS Reaction. *New J. Chem.* **2021**, *45*, 22444.
(83) Akamatu, H.; Satô, K. On the Catalytic Decomposition of Carbon Monoxide by Iron. *Bull. Chem. Soc. Jpn.* **1949**, *22* (3), 127−131.
(84) Kehrer, V. J. J.; Leidheiser, H. J. The Catalytic Decomposition of Carbon Monoxide on Large Metallic Single Crystals. *J. Phys. Chem.* **1954**, *58* (7), 550−555.

https://doi.org/10.1021/acsomega.3c10332
ACS Omega 2024, 9, 22607−22618